

DNS of scalar transfer across an air-water interface during inception and growth of Langmuir circulation



Amine Hafsi^a, Andrés E. Tejada-Martínez^{a,*}, Fabrice Veron^{a,b}

^a Department of Civil and Environmental Engineering, University of South Florida, Tampa, FL, USA

^b College of Earth, Ocean & Environment, University of Delaware

ARTICLE INFO

Article history:

Received 2 January 2017

Revised 16 June 2017

Accepted 23 June 2017

Available online 1 July 2017

Keywords:

Direct numerical simulation

Small scale Langmuir circulation

Scalar transfer

ABSTRACT

Direct numerical simulations (DNS) of an initially quiescent coupled air-water interface driven by an air flow with free stream speed of 5 m/s have been conducted. The DNS solves a scalar advection-diffusion equation for dissolved gas (or scalar) concentration in order to determine the impact of the water-side turbulence on scalar transfer from the air side to the water side and subsequent vertical transport in the water column. Two simulations are compared: one with a freely deforming interface and a second one with a flat interface. In the first simulation, the deforming interface evolves in the form of gravity-capillary waves generating aqueous Langmuir turbulence characterized by small-scale (centimeter-scale) Langmuir cells (LCs). The second simulation is characterized by pure shear-driven turbulence in the absence of LCs as the interface is intentionally held flat. It is concluded that the Langmuir turbulence serves to enhance vertical transport of the scalar in the water side and in the process it increases scalar transfer efficiency relative to the shear-dominated turbulence in the flat interface case. Furthermore, transition to Langmuir turbulence was observed to be accompanied by a spike in scalar flux characterized by an order of magnitude increase. These episodic flux increases, if linked to gusts and overall unsteadiness in the wind field, are expected to be an important contributor in determining the long-term average of the air-sea gas fluxes. The effectiveness of popular transfer velocity models, namely the small eddy model and the surface divergence model, in predicting this spike is evaluated via the DNS.

© 2017 Published by Elsevier Ltd.

1. Introduction

In the last few decades, our planet has been undergoing drastic changes to its carbon cycle which is the main cause of global warming. This is attributed to the dramatic increase of greenhouse gases such as carbon dioxide (CO₂) in the atmosphere due to the increasing industrialization of our societies. Greenhouse gases absorb solar energy and release it into the atmosphere, a process that keeps our planet warmer than it would be without the presence of these gases. A significant portion of these greenhouse gases interacts with the oceans because of the fact that oceans take up more than 70% (the majority) of the surface of the earth. The United States Environmental Protection Agency (EPA) suggests that CO₂ represents the majority (84%) of all greenhouse gases generated by human activities. Furthermore, about 30% to 40% of anthropogenic CO₂ is taken up by the oceans [3]. The accuracy of this latter assumption is arguable however given how difficult it is to predict and field measure gas transfer rates across wind-driven air-sea in-

terfaces due to the infinitesimal sizes of adjacent molecular sublayers below and above the interface. For example, on the water side in the absence of wave-breaking, the molecular sublayer underneath the air-water interface in lakes and oceans can be on the order of millimeters (see Fig. 1). As such it is important to understand the dynamics of gas transfer across molecular sublayers in order to develop new or test existing parameterizations of the transfer.

During low wind speeds (1–2 m/s), in the absence of wave-breaking, surface wave-current interaction in lakes and oceans leads to the generation of Langmuir turbulence characterized by small scale (centimeter-scale) Langmuir cells or LCs. As seen in the sketch of Fig. 2 (left panel), LCs consist of parallel counter-rotating vortices roughly aligned in the direction of the wind. It is well-known that LCs result from the interaction between the Stokes drift velocity induced by surface waves and the wind-driven shear current. It is also well-known that in the absence of breaking surface waves, the water side (aqueous) turbulence and associated eddies control gas transfer of sparingly soluble gases such as CO₂ from the air to the water. This is due to the fact that the diffusivity of sparingly soluble gases is three to four orders of magni-

* Corresponding author.

E-mail address: aetejada@usf.edu (A.E. Tejada-Martínez).

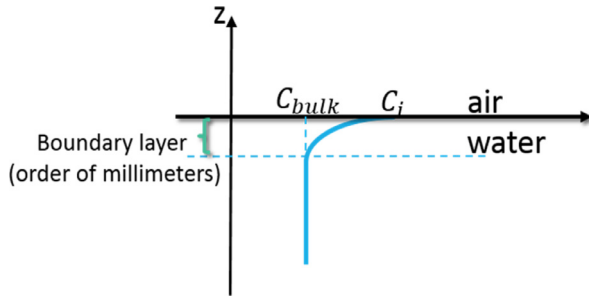


Fig. 1. Boundary layer in terms of dissolved gas (scalar) concentration in the water side below the air-water interface. C_i is the concentration at the air-water interface and C_{bulk} is the concentration in the bulk of the water column.

tude smaller in water than in air. The water-side turbulent eddies impinge on the molecular sublayer (sketched in Fig. 1) leading to an increase in gas concentration gradient across the layer and ultimately an increase of gas transfer through molecular diffusion. As noted by Veron and Melville [15], Langmuir turbulence and associated small scale LCs may serve this purpose. For example, in the laboratory experiments of Veron and Melville [15] of a wind-driven air-water interface, the inception of small scale LCs and subsequent transition to Langmuir turbulence (prior to the onset of micro-breaking wind waves) lead to a sudden spike in gas transfer velocity, a measure of the gas transfer efficiency from the air side to the water side. Transition to Langmuir turbulence refers to when the initially coherent vortices become unstable and loose coherency as they start to interact with each other nonlinearly.

Further evidence that Langmuir turbulence may have a strong impact on surface molecular boundary layers comes from surface temperature images during the presence of small scale LC in the experiments of Veron and Melville [15]. The panel on the right in Fig. 2 shows one of these surface temperature images with red indicating warmer temperatures and blue indicating colder temperatures. The presence of the Langmuir cells is manifested through the pattern in surface temperature. For example, the red temperature streaks coincide with the surface divergence zones of the Langmuir cells and vice-versa. Note that the surface divergence zones coincide or are directly above the upwelling limbs of the cells (see left panel of Fig. 2). Under a constant surface cooling heat flux, the upwelling limbs of the cells (see left panel of Fig. 2) impinge on the surface molecular sublayer, leading to a thinning of the layer and thus an increase in the surface temperature in order for the vertical temperature profile to satisfy the constant cooling flux. Similarly, the downwelling limbs of the cells lead to a decrease in surface temperature. Similar patterns in terms of scalar (gas) concentration at the air-water interface in the present DNS will be described further below.

The measurements of Veron and Melville [15] were collected under a gradually increasing wind with final speed of 5 m/s at a fetch of 10.72 m and during the presence of gravity-capillary waves possessing wavelengths up to 10–15 cm. More recent experiments made with sub-surface particle image velocimetry and surface infrared radiometry were conducted in a larger air-sea interaction facility at the University of Delaware [4]. Several wind forcings were studied in order to obtain a variety of LC scales and intensities. It was found that the LCs provide intense renewal of surface water with water from below. Consequently, the LCs rapidly transport surface layers to depth transporting momentum and scalars away from the surface at rates much larger than that of molecular diffusion.

Komori et al. [7] performed a DNS similar to the laboratory setting of Veron and Melville [15]. In their DNS, LC-like structures coexisting with micro-breaking capillary waves riding on larger

gravity-capillary waves could be identified. However, a study of LC-like structures and their connection with gas transfer efficiency across the air-water interface was not explored. More recently, DNS of Takagaki et al. [12], with configuration similar to that of Komori et al. [7], established that the turbulence of smaller scale than the LCs (and not the Langmuir turbulence as previously thought) is the primary disruptor of the surface molecular sublayer and thus the primary factor in driving scalar transfer across the air-water interface by molecular diffusion.

In the present study, DNS of a wind-driven coupled air-water interface is revisited focusing on the vertical transport induced by the small scale LCs. More specifically, the focus is on transfer velocity, a measure of the scalar transfer efficiency. Transfer velocity is not only defined in terms of the scalar vertical flux across the air-water interface via molecular diffusion, but also in terms of the difference in scalar concentration at the air-water interface and the concentration in the bulk region of the flow on the water side (see panel on left in Fig. 2). The importance of LCs in determining the transfer velocity will be elucidated through its efficient vertical mixing of scalar throughout the water side affecting the scalar concentration in the bulk region of the flow. Furthermore, popular transfer velocity models, namely the surface divergence model [10] and the small eddy model [1] that are based on the local turbulence state, will be evaluated, in particular their ability to predict the spike in scalar transfer induced by the transition to Langmuir turbulence observed in the present DNS and previously in the laboratory measurements of Veron and Melville [15] and Hafsi et al. [4].

2. DNS equations

The DNS equations consist of the incompressible continuity and the Navier-Stokes equations

$$\frac{\partial u_i}{\partial x_i} = 0 \quad (1)$$

$$\frac{\partial u_i}{\partial t} + u_j \frac{\partial u_i}{\partial x_j} = -\frac{1}{\rho} \frac{\partial p}{\partial x_i} + \nu \frac{\partial^2 u_i}{\partial x_j^2} \quad (2)$$

where u_i denotes the velocity field ($i=1,2$ and 3 represent the streamwise (or downwind), spanwise and vertical components, respectively), p is the pressure field, ν is the molecular kinematic viscosity and ρ is the density. In addition to the continuity and momentum (Navier-Stokes) equations to predict air and water flow velocities and pressures, the concentration of dissolved scalar (i.e. gas) in air and in water is predicted via a scalar transport equation:

$$\frac{\partial C}{\partial t} + u_j \frac{\partial C}{\partial x_j} = \kappa \frac{\partial^2 C}{\partial x_j^2} \quad (3)$$

where C is the concentration of the scalar and κ is the molecular diffusivity of the scalar. In this study, as has been done in others, the ratio ν/κ or Schmidt number (Sc) is set to 1 because this does not affect the fundamental turbulent mechanisms promoting scalar transfer and transport.

The computational solver used in this research is based on the open source numerical collection of C++ libraries OpenFOAM (Open source Field Operations and Manipulations) which uses the finite volume method to discretize the continuity, Navier-Stokes and passive scalar equations. The diffusion terms in these equations are discretized using a linear interpolation scheme whereas the advective terms are discretized using the limited Van Leer scheme [14], and the Euler method was used for temporal discretization.

After the discretization of the Navier-Stokes equations, the resulting pressure-velocity coupling for the momentum equation is

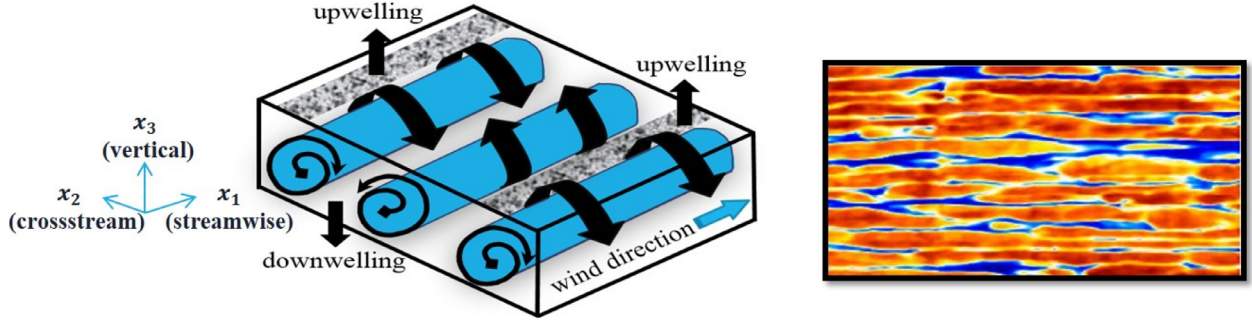


Fig. 2. Sketch of LCs on the left and surface manifestation of LCs on the air-water interface in terms of temperature on the right in the experiments of Veron and Melville [15]. On the panel on the left, LCs are characterized by upwelling and downwelling limbs consisting of regions of positive and negative vertical velocity fluctuations. The downwelling limbs emanate from the surface convergence of the cells and the upwelling limbs lead into to the surface divergence zones of the cells. On the panel on the right, the low temperature streaks (blue) are aligned in the streamwise direction coinciding with the surface convergence zones of the LCs. (For interpretation of the references to colour in this figure legend, the reader is referred to the web version of this article.)

resolved using PIMPLE method which is a combination of the Pressure Implicit with Splitting of Operators (PISO) method [9] and the Semi-Implicit Method for Pressure-Linked Equations (SIMPLE) method [11].

InterFOAM, a solver included with OpenFOAM, is used in order to track the air-water interface via a modified Volume of Fluid (VoF) multiphase methodology. In this study two fluids are considered (i.e., water and air). Denoting subscript “w” for water and “a” for air, the VoF methodology is expressed via the following equation for volume phase fraction, γ :

$$\frac{\partial \gamma}{\partial t} + \nabla \cdot (\gamma \mathbf{U}) + \nabla \cdot [(\mathbf{U}_w - \mathbf{U}_a) \gamma (1 - \gamma)] = 0 \quad (4)$$

Fluid velocity \mathbf{U} (u_i), density ρ and viscosity μ are expressed as

$$\mathbf{U} = \mathbf{U}_w \gamma + \mathbf{U}_a (1 - \gamma) \quad (5)$$

$$\rho = \rho_w \gamma + \rho_a (1 - \gamma) \quad (6)$$

$$\mu = \mu_w \gamma + \mu_a (1 - \gamma) \quad (7)$$

where $\gamma = 1$ for water (i.e., this value corresponds to a cell with 100% of its volume occupied by water) and $\gamma = 0$ for air (i.e., this value corresponds to a cell with 100% of its volume occupied by air). Thus \mathbf{U}_w and \mathbf{U}_a are the fluid velocities in water and in air, respectively, ρ_w and ρ_a are densities of water and air, respectively and μ_w and μ_a are dynamic viscosities of water and air, respectively.

The above VoF methodology follows the original methodology of Hirt et al. [5] while incorporating a compression flux term (the 3rd term on the left hand side of Eq. (4)) to lessen the effects of numerical smearing of the interface between the two phases [2] and therefore improve sharpness of the interface.

3. Computational setup

Simulations conducted follow closely the DNS of Komori et al. [7] of wind-driven, coupled air-water molecular boundary layers with a free nonlinearly deformable water surface (air-water interface). The juxtaposed domains of the air and water fluids along an initially flat air-water interface are represented by rectangular boxes with depths of δ and 2δ respectively, where $\delta = 1.25$ cm, while the streamwise and spanwise lengths are 8δ and 4δ respectively (see Fig. 2a). A Cartesian coordinate system was adopted where the streamwise and spanwise directions are given by the x -axis and the y -axis respectively, while the z -axis spans the air

and water depths (see computational domain in Fig. 3). Note that following the indicial notation introduced earlier in Eqs. (1)–(3), $x_1 = x$, $x_2 = y$ and $x_3 = z$.

The computational mesh shown in Fig. 3a consisted of 200 by 100 by 60 grid points on the air side and 200 by 100 by 120 grid points on the water side in the streamwise, spanwise and vertical directions respectively. The computational mesh is uniform along the streamwise and spanwise directions, while a gradual mesh refining scheme was applied in which the vertical mesh size becomes smaller in the approach to the air-water interface from either the water side or the air side. This meshing scheme was purposely used to resolve the air-water interface including centimeter-scale interfacial deformations as well as the molecular sub-layers in the air- and water-sides. The grid resolution for this mesh is between approximately 0.0006 cm (near the air-water interface) and 0.05 cm (near the top and bottom of the domain).

Boundary conditions are summarized in Fig. 3b. The water side was started from rest with a flat air-water interface driven from above by the sudden imposition of a pre-computed, fully-developed boundary layer airflow driven by a pressure gradient (Fig. 4a). This boundary layer airflow was pre-computed (as a first step) in a separate simulation with a no-slip bottom and a zero-shear stress condition on top while maintaining periodic boundary conditions elsewhere (along streamwise and spanwise boundaries). The pre-computed airflow was characterized by far-field mean velocity $U_\infty = 5$ m/s which is the same as the final far-field wind speed in the experiments of Veron and Melville [15]. For consistency, the computational mesh to run the preliminary airflow simulation was made identical to the air side portion of the air-water mesh in Fig. 3a.

The simulated Reynolds number based on U_∞ , and the height of the air column, δ , is 4160. The Reynolds number based on the air-side friction velocity at the air-water interface, u_τ , and δ is 200. Given this modest Reynolds number, we have ensured that the distances from the air-water interface to the closest grid points on the water and air sides, Δz , are less than $\Delta z^+ = 1$, where $\Delta z^+ = u_\tau \Delta z / \nu$ with u_τ and ν being the friction velocity and kinematic viscosity, respectively, in the water side or air side. As such, the air and water-side regions near the air-water interface have DNS-level resolution and do not require a subgrid-scale model. Thus we refer to the simulation methodology as DNS in light of the fact that the focus of our analysis is on the water-side turbulence precisely in the well-resolved region near the interface.

The initial condition for scalar concentration was $C = 1$ mol/m³ in the air side and $C = 0$ in the water side. At the top of the domain (at the top of the air side) C was set to 1 mol/m³ and at the bottom of the domain (the bottom of the water side) C was set to

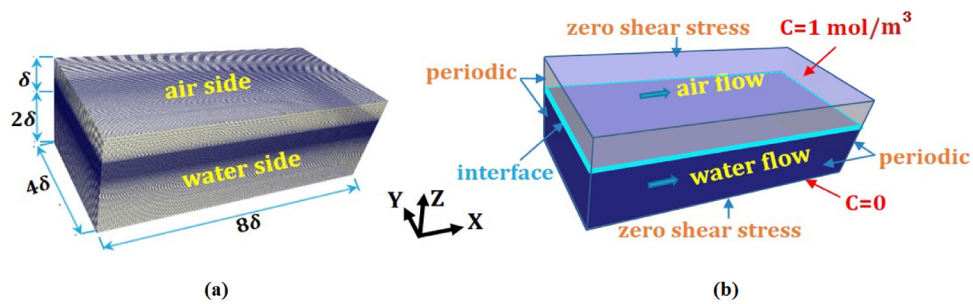


Fig. 3. (a) Coupled air-water flow domain and computational mesh and (b) flow domain and boundary conditions: Zero shear stress with zero normal flow and prescribed scalar concentration at top and bottom of the domain; periodicity in streamwise and spanwise directions.

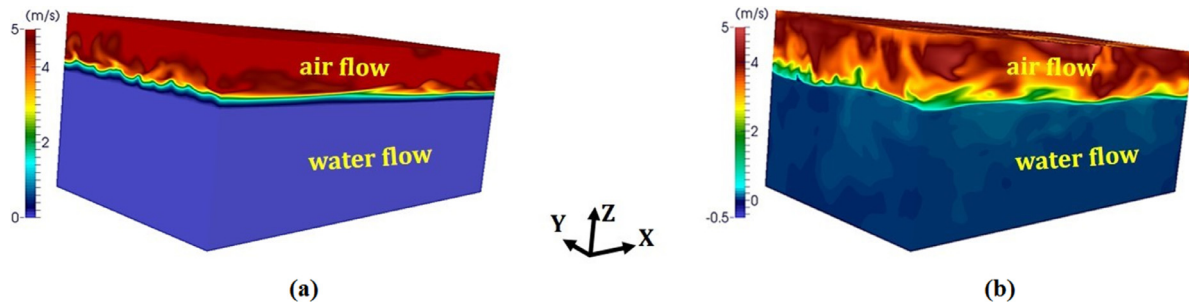


Fig. 4. (a) Instantaneous snapshot of streamwise (x) velocity field distribution within the domain showing the turbulence in action within the air side and the water at rest as initial conditions. (b) Instantaneous snapshot of streamwise velocity field distribution within the domain showing turbulence in action within both the air and water sides after 5 s. (For interpretation of the references to colour in this figure legend, the reader is referred to the web version of this article.)

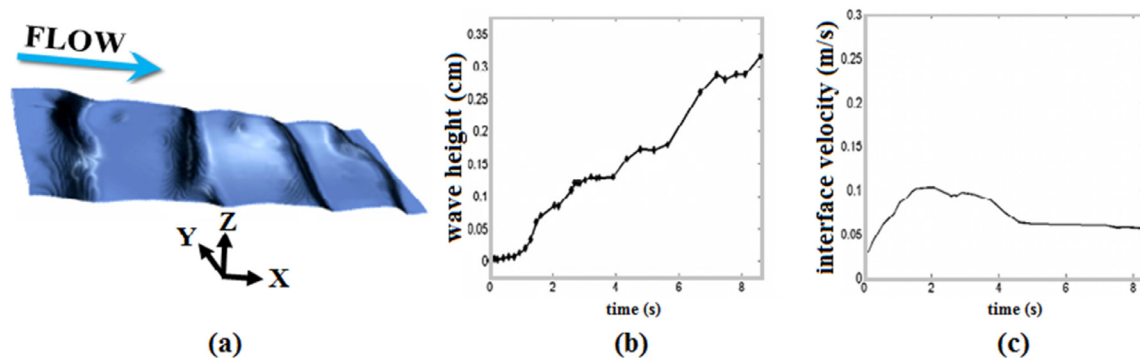


Fig. 5. Left panel: the instantaneous air-water interface in DNS at $t=2.5$ s. Middle panel: time series of the simulated maximum air-water interfacial wave heights. Right panel: time series of the simulated average streamwise velocity on the air-water interface. (For interpretation of the references to colour in this figure legend, the reader is referred to the web version of this article.)

0, ensuring saturated conditions on the water side and thus a flux of scalar from the air side to the water side (Fig. 3b).

4. Results

Fig. 4b shows an instantaneous snapshot of streamwise (x) velocity field distribution within the domain showing the turbulence in action within both the air side and the water side at $t=5$ s. Note that the air flow velocities are much higher than the water flow velocities as expected.

Soon after the simulation started, at time $t=1.5$ s, the air-water interface was characterized by short gravity-capillary waves as small as one centimeter in wavelength and 0.25 mm in height. Riding on these longer waves were capillary ripples with length scales of approximately 1 to 2 mm. Fig. 5a shows a snapshot of the air-water interface deformation (corresponding to simulation time $t=2.5$ s) of the DNS revealing gravity-capillary waves along with superimposed smaller capillary waves or ripples. During the simulation, time series of maximum wave height (twice the maximum of the wave amplitude) and averaged streamwise velocity on

the wavy interface (averaged over the interface) were recorded (see Fig. 5b and c). In addition to the gravity-capillary waves being non-uniform in the streamwise direction (as the capillary ripples populate only the forward face of the longer gravity-capillary waves), the gravity-capillary waves are also non-uniform in the spanwise direction. Thus the maximum amplitude time series corresponds to the maximum amplitude over the entire non-uniformly deformed air-water interface recorded at each time step. After a period of approximate exponential growth between $t=0$ and $t=1.8$ s, the wave continues to grow linearly reaching a wave height of ~ 0.3 cm in about 8 s (Fig. 5b). Meanwhile, the average streamwise velocity on the interface reaches a nearly constant value of approximately 0.07 m/s after 4 s (Fig. 5c). Both time series in Figs. 5b and 5c are in good agreement with the corresponding curves in the DNS of Komori et al. [7]. The interested reader is directed to Hafsi et al. [4] for more details on this comparison.

As can be seen in Fig. 6a at $t=0.5$ s, streamwise velocity fluctuations on the interface are characterized by smooth (streamwise) downwind elongated streaks. These narrow streaks are found to be parallel to each other, while alternating in sign in the spanwise

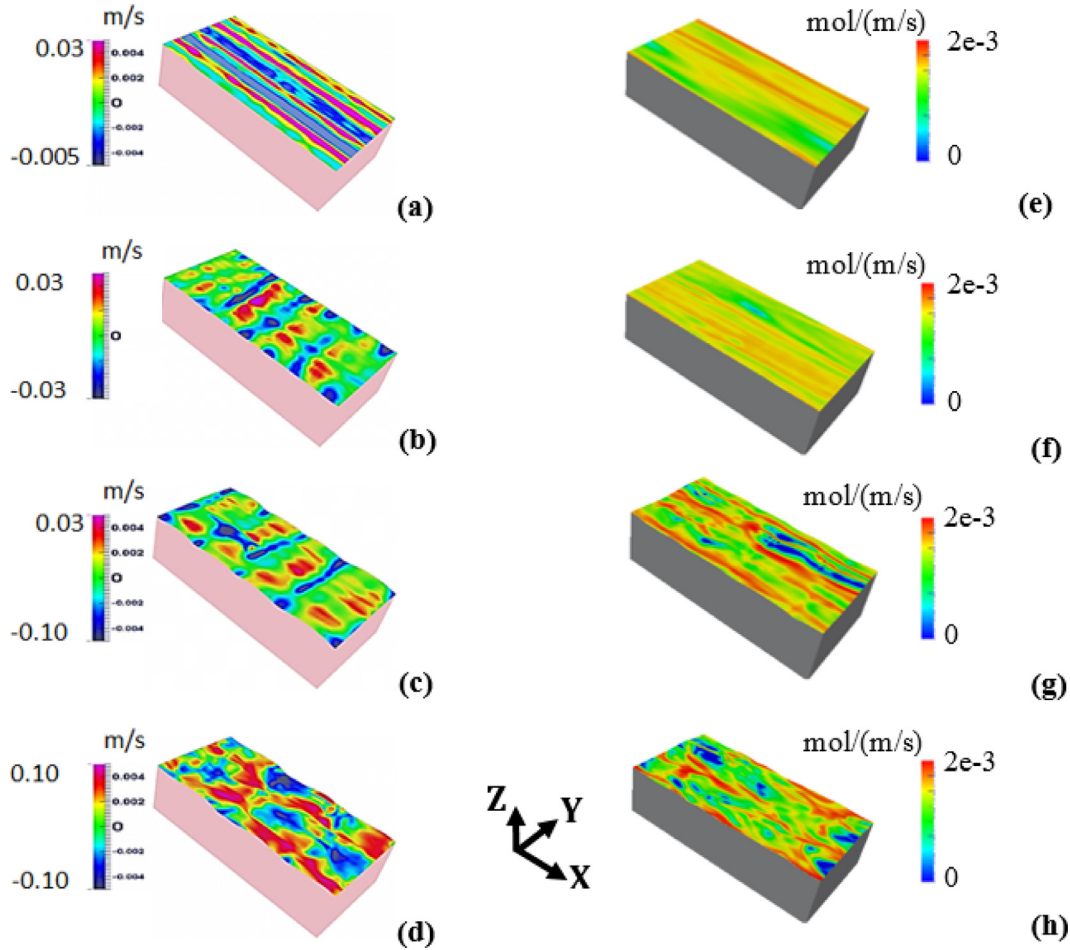


Fig. 6. Instantaneous streamwise velocity fluctuation at (a) $t = 0.5$ s, (b) $t = 1$ s (c) $t = 2.5$ s and (d) $t = 4$ s. Instantaneous scalar flux in mol/(m/s) at (e) $t = 0.5$ s and (f) $t = 1$ s (g) $t = 2.5$ s and (h) $t = 4$ s. (For interpretation of the references to colour in this figure legend, the reader is referred to the web version of this article.)

direction. The positive streaks correspond to the surface convergence zones of the small scale LCs resolved. Thus the LCs result in an acceleration of the local downwind bulk flow over the surface convergence zone of the cells, as described by Thorpe [13]. Starting at approximately $t = 1$ s (Fig. 6b), the streaky structure of the streamwise velocity fluctuation is disrupted by capillary wave interfacial deformations until about $t = 2.5$ s (Fig. 6c). This observed disruption is due to the fact that the downwind velocity fluctuation not only has a component due to the turbulence but it also has a significant capillary wave-induced component. This is typical of turbulent flow fields on or below surface waves for which the velocity fluctuations may be decomposed in terms of a component due to the turbulence plus a component due to the waves (i.e. an orbital component) (e.g. see [8]). As time progresses after $t = 2.5$ s, (e.g. at $t = 4$ s, Fig. 6d) the downwind elongated streaks re-emerge, due to the turbulent component of the velocity becoming more dominant than the wave-induced component. Re-emergence of downwind elongated streaks is indicative of the flow transitioning to Langmuir turbulence.

Fig. 6e–h shows instantaneous scalar molecular fluxes at the air-water interface at $t = 1$ s, $t = 2.5$ s, $t = 4$ s and $t = 6$ s. This flux can be obtained as

$$F = \kappa \nabla C \cdot \mathbf{n} \tag{8}$$

evaluated at the air-water interface, where \mathbf{n} is the normal to the interface. As seen in Fig. 6e–h, the flux shows an increase for times greater than $t = 2.5$ s, attributed to the transition to Langmuir turbulence previously described. Note that the flux is characterized by

streaks similar to the velocity fluctuations presented earlier, suggesting strong correlation between the Langmuir turbulence and the flux. Specifically, as the upwelling limbs of the LCs impinge on the diffusive sublayer of the scalar, the upwells reduce the thickness of this layer serving to locally increase the vertical gradient of the scalar concentration across the layer and ultimately the scalar flux. This is manifested in the streamwise-elongated streaks of high flux observed in Fig. 6e–h, which are situated above the upwelling limbs of the streamwise-elongated LCs (sketched in the left panel of Fig. 2).

Additionally, we compare results in terms of instantaneous streamwise vorticity in our simulation with the deforming air-water interface (described above) with instantaneous streamwise vorticity coming from a similar simulation but with the air-water interface held fixed (flat). The vorticity in the former case is characterized by the presence of the wave and wind-driven Langmuir turbulence and associated Langmuir cells, while the LCs are absent in the latter case and the turbulence is purely shear-driven. The results from the flat interface case are shown in Fig. 7a and b and the results from the deforming interface case are shown in Fig. 7c and d. The deforming interface case is characterized by Langmuir cells manifested through coherent streamwise vortical structures growing in the cross-stream direction and in depth whereas the simulation with the flat interface shows smaller and less intense near-surface vortices.

In both deforming interface and flat interface simulations, the air-side was saturated with the scalar whereas the water side had zero scalar concentration as the initial condition. Thus in both

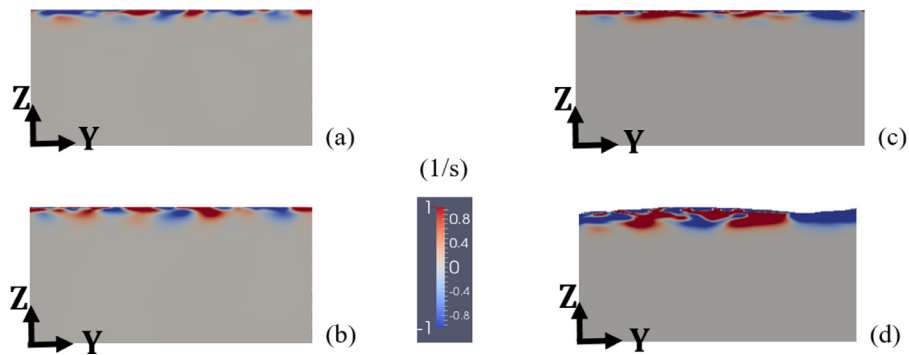


Fig. 7. Instantaneous streamwise vorticity (1/s) from DNS with air-water interface held flat (without Langmuir turbulence) at (a) $t=1$ s and (b) $t=3$ s. Instantaneous streamwise vorticity (1/s) from DNS with freely deforming air-water interface (with Langmuir turbulence and associated LCs) at (c) $t=1$ s and (d) $t=3$ s. (For interpretation of the references to colour in this figure legend, the reader is referred to the web version of this article.)

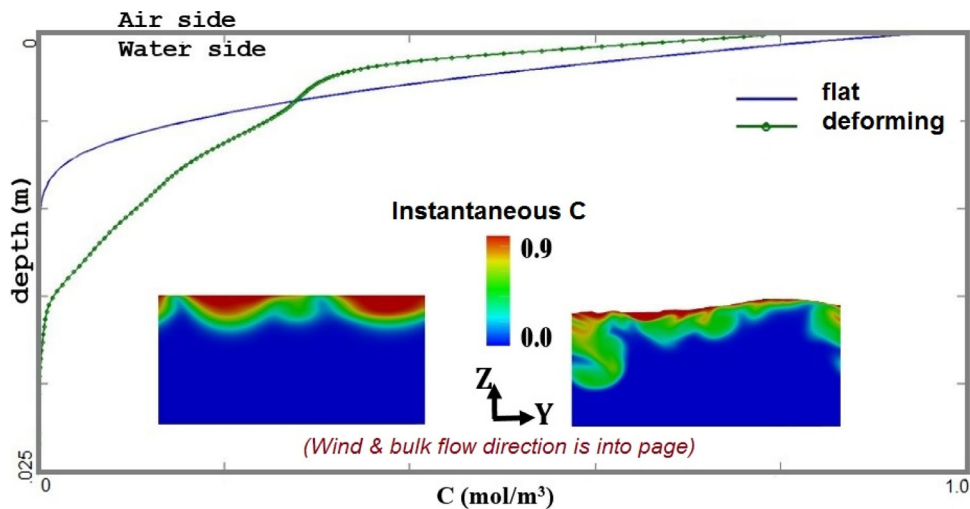


Fig. 8. Depth profiles (averaged over streamwise and spanwise directions) and instantaneous snapshots of scalar concentration at time $t=4$ s in the simulation with a deforming interface (with Langmuir turbulence and associated LCs) and the simulation with a flat interface (without Langmuir turbulence). (For interpretation of the references to colour in this figure legend, the reader is referred to the web version of this article.)

cases, the scalar flux was from the air side to the water side. Prior to the transition to Langmuir turbulence which was previously determined to be at approximately $t=2.5$ s for the deforming interface case, both cases simulated (flat and deforming interface simulations) were compared in terms of depth profiles of mean (i.e. horizontally-averaged) scalar concentration in the water column. It was found that both cases possess similar concentration profiles through $t=2.5$ s (not shown). However, for times greater than 2.5 s, the Langmuir turbulence and associated Langmuir cells in the deforming interface case generate greater vertical transport than the purely shear generated turbulence in the flat interface case. From the depth profiles and instantaneous contours of scalar concentration shown in Fig. 8, we can conclude that the Langmuir turbulence penetrates deeper than the shear turbulence thus the Langmuir turbulence is able to transport higher concentration fluid from the surface to greater depths. Note that as time progresses the difference between Langmuir turbulence penetration in the deforming interface case and the shear turbulence penetration in the flat interface case becomes more significant.

The spatially averaged scalar flux across the air-water interface (averaged over the interface) for the flat and deforming interface cases are shown in Fig. 9. A dramatic explosion or spike of scalar flux is observed in the deforming case at approximately $t=2.5$ s when the flow transitions to Langmuir turbulence. In contrast, this sudden increase in scalar flux is noticeably absent in the flat interface case. After this spike, the average scalar flux obtained in

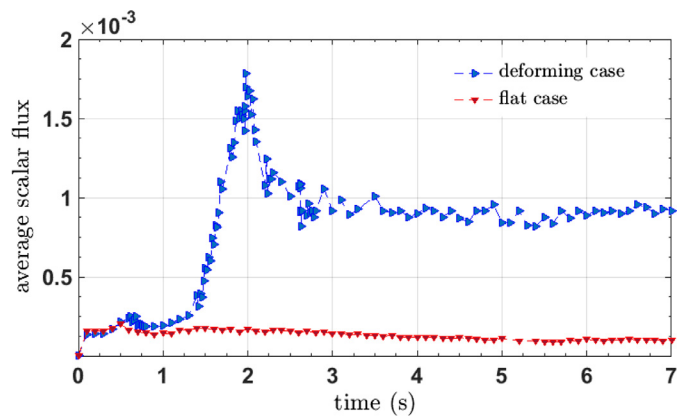


Fig. 9. Average scalar flux through the air-water interface. (For interpretation of the references to colour in this figure legend, the reader is referred to the web version of this article.)

the deforming case decreases significantly but stabilizes at a mean value approximately five times greater than the scalar flux obtained in the flat case. In real oceans and lakes, it is likely that such gas flux spikes are correlated with wind transients or gusts and thus might be a dominant contributor to the long-term time-averaged gas flux.

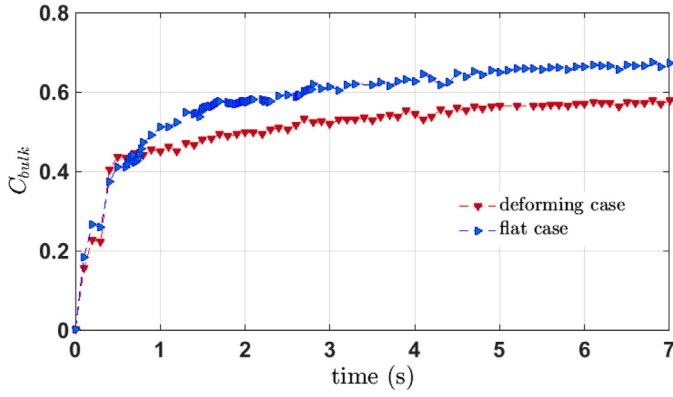


Fig. 10. Bulk concentration of the air-water interface. (For interpretation of the references to colour in this figure legend, the reader is referred to the web version of this article.)

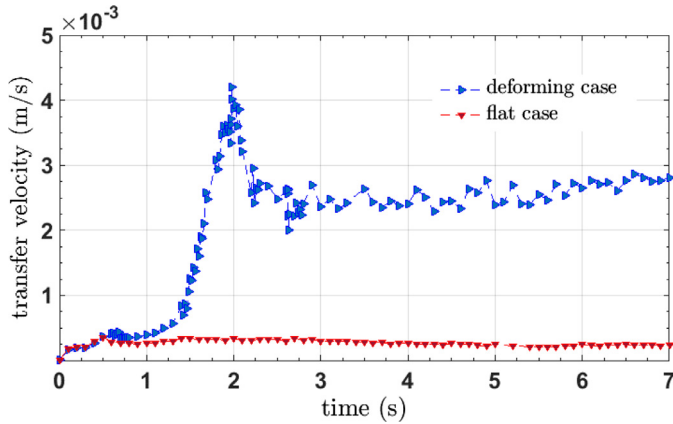


Fig. 11. Transfer velocity. (For interpretation of the references to colour in this figure legend, the reader is referred to the web version of this article.)

Next, we calculate transfer velocity, a measure of scalar transfer efficiency, following Kader and Yaglom [6]:

$$k_L = \kappa \frac{\nabla C \cdot \mathbf{n}}{(C_i - C_{bulk})} \quad (9)$$

where C_i is streamwise and spanwise average concentration on the interface and C_{bulk} is bulk concentration calculated as

$$C_{bulk} = \int_0^{2\delta} \langle C \rangle_{x,y} \langle u_1 \rangle_{x,y} dz \quad (10)$$

with $\langle \cdot \rangle_{x,y}$ denoting the average over streamwise and spanwise directions. Due to the enhanced vertical transport induced by the Langmuir turbulence and associated cells, the bulk concentration is greater in the interface deforming case compared to the flat interface case (Fig. 10). Ultimately this leads to a greater transfer velocity (k_L) in the deforming interface case (Fig. 11), as k_L is inversely proportional to the difference between concentration at the interface and bulk concentration (Eq. 9).

In the field, direct evaluation of scalar flux via Eq. (8) is impractical and instead following Eq. (9), the flux is evaluated as a parameterized transfer velocity multiplied by the difference in concentration at the interface and the bulk, $C_i - C_{bulk}$. Surface renewal theory is one of the widely accepted theories used to obtain parameterizations of transfer velocity. Surface renewal theory is based on the principle that turbulent eddies intermittently bring up low concentration fluid packages close to the surface from below. According to surface renewal theory, transfer velocity can be obtained or parameterized as

$$k_L = (\kappa/\tau)^{1/2} \quad (11)$$

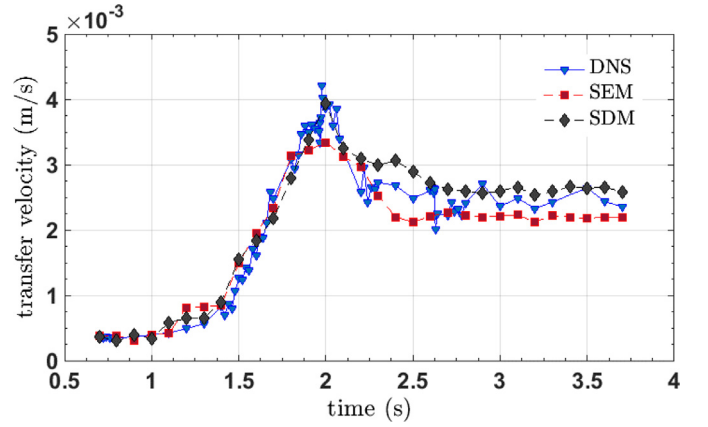


Fig. 12. Comparison of transfer velocity in the DNS (defined in Eq. (7)) with modelled transfer velocity predicted via the SEM in Eq. (14) and via the SDM in Eq. (17). (For interpretation of the references to colour in this figure legend, the reader is referred to the web version of this article.)

where τ is the surface renewal turbulent time scale. Assuming that small near-surface eddies control the surface renewal, Banerjee et al. [1] proposed a parameterization of τ in terms turbulent kinetic energy dissipation rate ε at the surface defined as

$$\tau \propto (\nu/\varepsilon)^{1/2} \quad (12)$$

where ε is defined as

$$\varepsilon = \nu \left\langle \frac{\partial u'_i}{\partial x_j} \frac{\partial u'_i}{\partial x_j} \right\rangle_s \quad (13)$$

with the derivatives evaluated at the water surface (i.e. the air-water interface), u'_i denoting the velocity fluctuation and $\langle \cdot \rangle_s$ denoting averaging over the water surface. Inserting (13) into (12) and using (11) leads to the small eddy model (SEM) with a parameter or coefficient due to the proportionality in (12):

$$k_L = 0.419(\varepsilon\nu)^{1/4} Sc^{-1/2} \quad (14)$$

The constant of proportionality, 0.419, was determined by Zappa et al. [17] using a large field experimental data set collected under a wide range of wind and wave conditions.

An alternative surface renewal time scale was proposed by McCready et al. [10] in terms of surface divergence as

$$\tau \propto \langle \beta^2 \rangle_s^{-1/2} \quad (15)$$

where the surface divergence β corresponds to

$$\beta = -\frac{\partial u'_n}{\partial n} \quad (16)$$

evaluated at the water surface with n corresponding to the direction along the unit normal to the surface and u'_n corresponding to the fluctuation of the velocity component normal to the surface. Inserting (16) into (15) and using (11) leads to the surface divergence model (SDM)

$$k_L = 0.71\nu^{1/2} \langle \beta^2 \rangle_s^{1/4} Sc^{-1/2} \quad (17)$$

with 0.71 being the constant of proportionality associated with (15). The constant of proportionality was determined empirically by McCready et al. [10].

Using the results of the DNS it was possible to investigate the accuracy of the SEM and the SDM, especially their prediction of the spike in transfer velocity during the transition of the flow to Langmuir turbulence. As seen in Fig. 12, prior to this transition both models agree well with the DNS. The peak of the transfer velocity is best predicted by the SDM whereas the SEM underpredicts the peak by 19%. After the peak, the SDM slightly overpredicts while the SEM underpredicts the transfer velocity.

5. Summary and conclusion

Scalar transport results were presented from DNS of a wind driven air-water interface with resolution of gravity-capillary waves, capillary ripples riding on the longer waves and molecular sublayers below and above the interface. Transfer of scalar from the air to the water side was ensured by saturating the air side with the scalar. It was seen that the deforming interface and associated aqueous Langmuir turbulence plays an important role in determining vertical transport of the scalar throughout the water side. Vertical transport induced by the LCs was seen to enhance bulk concentration throughout the water column which ultimately enhances transfer velocity, a measure of scalar transfer efficiency. LCs rapidly transport surface layers to depth thereby transporting momentum and scalars away from the surface at rates much larger than shear-driven turbulence occurring when the air-water interface was intentionally held flat.

Transition to Langmuir turbulence was observed to be accompanied by a spike in scalar flux characterized by an order of magnitude increase. These flux increases, if linked to episodic gusts and unsteadiness in the wind field, are expected to be an important contributor in determining the long-term average of the air-sea fluxes. Thus, these results highlight a new (pressing) need of developing practical parameterizations of transfer velocity that can capture scalar flux spikes associated with transition to Langmuir turbulence on the sea surface during sudden wind gusts. Although parameterizations of the transfer velocity such as the SEM and SDM were seen to be able to capture the spikes, these parameterizations require knowledge of the turbulence, for example, in terms of the surface TKE dissipation rate and the surface divergence. More practical parameterizations of the transfer velocity have been developed in terms of easily accessible parameters such as wind speed [16], however, such a parameterization would not be able to capture the spike in scalar transfer as a result of the transition to Langmuir turbulence. In the cases studied here, the spike in scalar flux occurred during transition to turbulence while the mean far-field wind speed was constant at 5 m s^{-1} , thus the wind speed would not be able to serve as a proxy for the spike in transfer velocity.

Finally, recent DNS studies by Takagaki et al. [12] have shown that the surface shear turbulence of smaller scale than the LCs is the primary factor in driving scalar transfer across the air-water interface via molecular diffusion. Nevertheless, the DNS case investigated here with gravity-capillary waves and associated Langmuir

turbulence is characterized by a spike in scalar transfer unlike the DNS case without waves and LCs (i.e. when the air-water interface is intentionally held flat). Furthermore, after the passage of the scalar flux spike, the scalar flux remained higher (by a factor of five) in the case with waves and LCs unlike the case with air-water interface held flat. Thus, future research should focus on understanding the cause of this and thus the influence of the waves on the small scale shear-turbulence (smaller than the LCs) that controls the scalar transfer across the air-water interface via molecular diffusion.

References

- [1] Banerjee S, Scott DS, Rhodes E. Mass transfer to falling wavy liquid films in turbulent flow. *Ind Eng Chem Fund* 1968;7:22–7.
- [2] Deshpande SS, Anumolu L, Trujillo MF. Evaluating the performance of the two-phase flow solver interFoam. *Comput Sci Discov* 2012;5 Article 014016.
- [3] Donelan MA, Wanninkhof R. Gas transfer at water surfaces—concepts and issues, 127. Washington D.C.: American Geophysical Union; 2002. p. 01–10.
- [4] Hafsi A, Ma Y, Buckley M, Tejada-Martínez AE, Veron F. DNS and measurements of scalar transfer across an air-water interface during inception and growth of Langmuir circulation. *IOP Conf Series* 2016;35:012006.
- [5] Hirt CW, Nichols BD. Volume of Fluid (VOF) method for the dynamics of free boundaries. *J Comput Phys* 1981;39:201–25.
- [6] Kader BA, Yaglom AM. Heat and mass transfer laws for fully turbulent wall flows. *J Heat Mass Transfer* 1972;15:2329–53.
- [7] Komori S, Kurose R, Iwano K, Ukai T, Suzuki N. Direct numerical simulation of wind-driven turbulence and scalar transfer at sheared gas-liquid interfaces. *J Turbulence* 2010;11 N32.
- [8] Magnaudet J, Thais L. Orbital rotational motion and turbulence below laboratory wind water waves. *J Phys Oceanogr* 1995;100(C1):757–71.
- [9] Márquez Damián S. An extended mixture model for the simultaneous treatment of short and long scale interfaces Ph.D. thesis. Facultad de Ingeniería y Ciencias Hidricas, Universidad Nacional del Litoral; 2013.
- [10] McCreedy MJ, Vassiliadou E, Hanratty TJ. Computer simulation of turbulent mass transfer at a mobile interface. *AIChE J* 1986;32(7):1108–15.
- [11] Patankar SV, Spalding DB. A calculation procedure for heat, mass and momentum transfer in three-dimensional parabolic flows. *Int J Heat Mass Transfer* 1972;15:1787.
- [12] Takagaki N, Kurose R, Tsujimoto Y, Komori S, Takahashi K. Effects of turbulent eddies and Langmuir circulations on scalar transfer in a sheared wind-driven liquid flow. *Phys Fluids* 2015;27:016603.
- [13] Thorpe SA. Langmuir circulation. *Annu Rev Fluid Mech* 2004;36:55.
- [14] Van Leer B. Towards the ultimate conservative scheme: II. *J Comput Phys* 1974;14:361–76.
- [15] Veron F, Melville WK. Experiments on the stability and transition of wind driven water surfaces. *J Fluid Mech* 2001;446:25–65.
- [16] Wanninkhof R. Relationship between wind speed and gas exchange over the ocean. *J Geophys Res* 1992;97:7373–82.
- [17] Zappa CJ, McGillis WR, Raymond PA, Edson JB, Hints EJ, Zemmelen HJ, et al. Environmental turbulent mixing controls on air-water gas exchange in marine and aquatic systems. *Geophys Res Lett* 2007;34:L10601.